

Vision Based Cone Angle Estimation of Bubbly Cavitating Flow and Analysis of Scattered Bubbles using Micro Imaging Techniques

Gokhan Alcan⁽¹⁾, Morteza Ghorbani⁽¹⁾, Ali Kosar⁽¹⁾, Mustafa Unel^{(1)*}

⁽¹⁾Mechatronics Engineering Program

Faculty of Engineering and Natural Sciences

Sabanci University, Orhanli, Tuzla, Istanbul, Turkey

{gokhanalcan,morteza,kosara,munel}@sabanciuniv.edu

Abstract—Hydrodynamic cavitation is an effective and alternative treatment method in various biomedical applications such as kidney stone erosion, ablation of benign prostatic hyperplasia tissues and annihilation of detrimental cells. In order to effectively position the orifice of bubbly cavitating flow generator towards the target and control the destructive cavitation effect, cone angle of multi-phase bubbly flow and distributions of scattered bubble swarms around main flow must be determined. This paper presents two vision based solutions to determine these quantities. 3D Gaussian modeling of multi-phase flow and edge slopes of cross-section are used to estimate the cone angle in a Kalman filter framework. Scattered bubble swarm distributions around main flow were assumed as a normal distribution and analyzed with the help of covariance matrix of the bubble position data. Hydrodynamical cavitating bubbles were generated from 0.45 cm long micro probe with 152 μ m inner diameter under 10 to 120 bars pressures and monitored via Particle Shadow Sizing technique. Proposed methods enabled to quantize the increasing inlet pressure effect on bubbly cavitating multi-phase flow.

I. INTRODUCTION

Sudden pressure drop down below the vapor pressure of the liquid results in vaporization and bubble generation. This phenomenon is called hydrodynamic cavitation. Generated bubbles in lower inlet pressure, may collapse when they are subjected to atmospheric pressure. Highly destructive shock waves are generated by the collapse of cavitation-caused bubbles. Continuous collision of solid surfaces and generated bubbles leads to cavitation erosion.

Destructive effect of hydrodynamic cavitation is normally undesirable and must be minimized in machines closely interact with liquids such as ships' propellers and hydraulic turbines [1]. Turning destructive effect into an advantage is possible in many biological and biomedical applications. In [2], hydrodynamic cavitation is used as a tool in kidney stone erosion. Prostate cells are killed and benign prostatic hyperplasia tissue is ablated by hydrodynamic cavitation in [3].

Several research studies in the past dealt with extraction of visual information by processing microscopic images and estimation of several important parameters associated with the underlying physical phenomenon [4], [5], [6]. Visualization and investigation of micro scale hydrodynamic cavitation requires

high-speed micro imaging techniques. Since Particle Image Velocimetry provides only velocity fields accurately by using laser as illumination source [7], LED is replaced with laser and particle shadow velocimetry is presented in [8]. Simultaneous velocity measurement and interface tracking in multi-phase flows through circular microchannels of 500 μ m diameter are investigated with the help of micro particle shadow velocimetry [9]. In addition to various visualization techniques, there exist several promising visual processing methods to investigate micro-nano scale bubbles in literature. [10] simulates the rising bubble as an ellipsoid consisting of two semi-ellipsoids up-down and 3D reconstruction of single rising bubble is implemented to describe the dynamic characteristic of bubbly flow. [11] proposes a two step method: contour segmentation and segment grouping for recognizing overlapping elliptical bubbles. In [12], an image analysis method is developed to analyze bubble size distributions between 2mm and 10mm.

In this paper, we present vision based solutions to requirements of bubbly cavitating flow usage in several biomedical applications. In order to position the orifice of bubbly flow generator effectively, Kalman filter based virtual cone angle estimation is presented. To control the destructive cavitation effect, scattered bubble swarms distributions around the main flow is analyzed by utilizing the covariance matrix of bubble positions data.

The organization of the paper is as follows: In Section II, the requirement of cone angle estimation and necessity of the determination of scattered bubble swarm around the main flow are mentioned and two proposed solutions are explained. In Section III, Particle Shadow Sizing setup is introduced as micro imaging technique. In Section IV, results related to cone angle estimation and scattered bubble swarm analysis are presented. Finally, paper is concluded with some remarks in Section V.

II. PROBLEM STATEMENT AND PROPOSED SOLUTIONS

During the process of hydrodynamic cavitation, multi-phase bubbly flow forms a virtual cone which starts with the orifice and extends through the flow. Soon after the orifice of hydrodynamic cavitation generator probe, scattered bubbles around main spray flow are observed. These initial bubbles are considered as the most destructive ones, since they have just originated and have not lost much speed in liquid yet.

*Corresponding author, e-mail: munel@sabanciuniv.edu

To manipulate the orifice of bubbly cavitating flow generator precisely and control the destructive effect of newborn bubbles and to estimate their operational area, generated virtual cone angle and scattered bubble distributions around main flow have to be determined.

A. Cone Angle Estimation

To estimate virtual cone angle, several image preprocessing steps and 3D Gaussian modeling are utilized. For robust estimation of the angle, a Kalman filter is also employed. Details of these procedures are provided below.

1) *Image Preprocessing*: Visualization of droplets individually after 11mm far from the orifice is possible as in Fig. 1(a), when inlet pressures (P_i) varies from 10 to 60 bars. Above 60 bars inlet pressures, observable droplets' sizes decrease under increasing pressures and small size droplets are monitored as thin fibers as in Fig. 1(b).

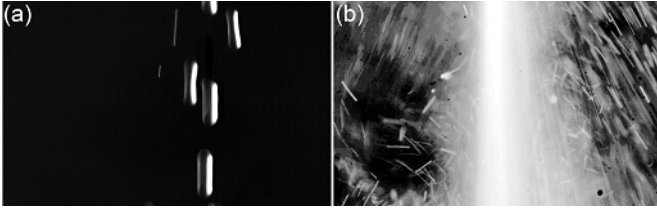


Fig. 1. (a)Detected droplets ($P_i=10$ bars) (b)Thin fiber visualization of small size droplets ($P_i=120$ bars)

Estimation of virtual cone's angle from a single instance frame can be unreliable due to the highly dynamic motion of cavitating flow. Therefore, a representative 3D structure of multi-phase bubbly flow is constructed for all pressure levels. This structure for the flows below 60 bars inlet pressure is obtained via super-imposition of detected individual droplets after a series of pre-processing techniques were applied.

Since droplets contain liquid and air in some portion inside, sparkles and reflections may occur during the visualization of their shadows. In unprocessed original images, droplets cannot be distinguished from background easily due to shadows, noises and undesired particles. Acquired data must be purified from the noises and enhanced for accurate droplet detection.

Pre-processing starts with contrast increment to make foreground to be distinguishable from background. If acquired image histogram values are very close to each other, it can still prevent the accurate droplet detection, so histogram equalization enhances the contrast by transforming the values of the image in the color map of indexed image. Before applying a final threshold to the image '*morphological opening*' operation, which is the dilation of the erosion of the image by a structuring element, is applied to get smoother and more distinguishable image. After applying Otsu's thresholding method [13], obtained binary image is labelled via connected component analysis. With the help of droplet shapes' eccentricities, labelled regions are filtered to eliminate non-droplet abnormal shapes.

2) *3D Gaussian Modeling*: After suitable droplet regions are extracted, their binary mask frames are superimposed consecutively and from blue to red image is constructed.

Obviously red regions represents the points where droplets exist more. This 2D gradient image encouraged to construct the 3D representation. Finally when all frames are superimposed, with the intuition of 3D representation, droplet flow cross-section can be modeled as Gaussian distribution (Fig. 4).

For inlet pressure levels higher than 60 bars, in each frame small size droplets are already monitored as superimposed. With the intuition of the process in lower pressure levels, after applying similar pre-processing steps, 3D representation of each frame was indeed a Gaussian distribution as expected (Fig. 2). Here Z-axis of the structure is determined by the intensity values of preprocessed shadow images where brighter intensities indicate the denser droplets regions.

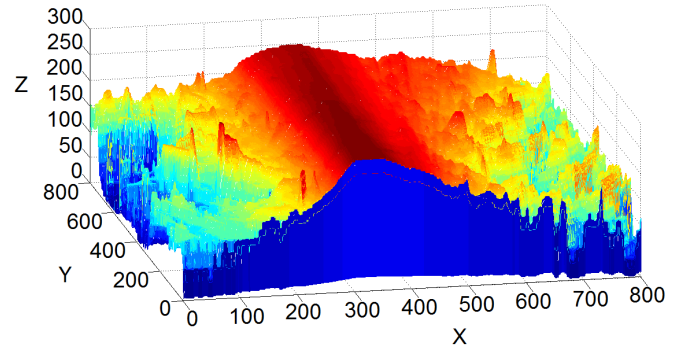


Fig. 2. 3D structure at higher inlet pressure levels

Below 60 bars inlet pressure, superimposition based structure's Gaussian properties are utilized to determine appropriate cross-sectional planes. Planes parallel to x-y plane and intersect with z plane are created to calculate the angle of droplet flow. It is observed that above Z_{max} and below Z_{min} levels, cross sectional area does not contain meaningful data. Gaussian function has remarkable data between the σ and 2σ as its nature, these levels are also related to the mean (μ) and standard deviation (σ) of the Gaussian function such that

$$Z_{max} = f(\mu \mp \sigma) \quad (1)$$

$$Z_{min} = f(\mu \mp 2\sigma) \quad (2)$$

High fidelity side edges in cross-section of 3D structure at Z level are used to calculate the cone angle where

$$f(\mu \mp \sigma) \leq Z \leq f(\mu \mp 2\sigma) \quad (3)$$

Cross-sectional image at Z level contains only edge points of flow, so best lines are fitted to these points by minimizing the sums of squares of perpendicular distances (geometric distance) from the data points to the line (Fig. 3).

The equation of the best line in polar coordinates is written as:

$$\sin(\alpha)x - \cos(\alpha)y = \rho \quad (4)$$

where ρ and α are the distance of the line from the origin and the angle between the line and positive x axis respectively. Slope of the line can be written from the line equation as:

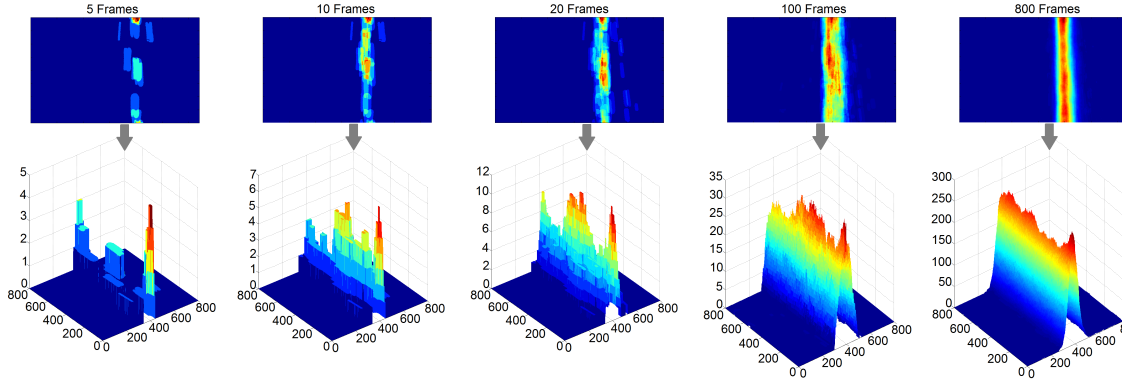


Fig. 4. Super-imposition of droplet masks

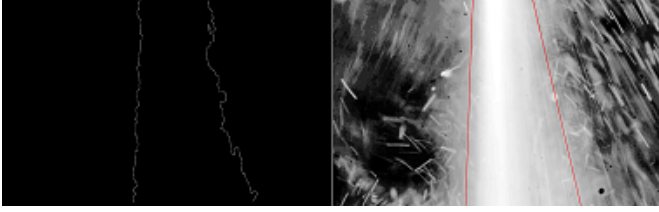


Fig. 3. Detected flow edges and best line fitting

$$m = -\frac{\sin(\alpha)}{-\cos(\alpha)} = \tan(\alpha) \quad (5)$$

Cross-section of 3D Gaussian shape gives left and right edge points, so two different lines are fitted. Angle between these two lines, i.e. cone angle, can be calculated as:

$$\theta = \arctan\left(\frac{m_1 - m_2}{1 + m_1 m_2}\right) \quad (6)$$

where m_1 and m_2 are the slopes of the lines and $m_1 > m_2$.

3) *Kalman Filter Estimation*: To estimate the cone angle more accurately, various cross-sections are taken at several Z levels of superimposed structure. Above 60 bars inlet pressure, instinctively acquired Gaussian structure is utilized in each frame and unlike lower inlet pressures, Z level is decided as constant which obeys (3). To increase the accuracy, in each frame cone angle is calculated. Since small size droplet based thin fibers form very noisy 3D structure, there exist sudden changes in angle calculations and it's seen that some of them are outliers. To prevent abrupt changes in angle calculations and estimate the angle by using the video sequence, the ubiquitous Kalman filter is implemented.

Cone angle (θ) of the flow is considered as the state, and angle calculations are taken as measurements. Thus, state and measurement models can be written as:

$$\theta(k+1) = \theta(k) + w(k) \quad (7)$$

$$z(k) = \theta(k) + v(k) \quad (8)$$

where $\theta(k)$ is the state of the process, $w(k)$ is the process noise, $z(k)$ is measurement and $v(k)$ is the measurement noise.

Process and measurement noises are modeled by additive zero mean Gaussian white noise with constant covariances C_w and C_v . The optimal state (i.e. cone angle) can be estimated by the following celebrated Kalman filter [14] algorithm:

$$\hat{\theta}(k+1|k) = \hat{\theta}(k) \quad (9)$$

$$P(k+1|k) = P(k) + C_w \quad (10)$$

$$K(k+1) = P(k+1|k) \left(P(k+1|k) + C_v \right)^{-1} \quad (11)$$

$$\hat{\theta}(k+1) = \hat{\theta}(k+1|k) + K(k+1) \left(z(k+1) - \hat{\theta}(k+1|k) \right) \quad (12)$$

$$P(k+1) = \left(I - K(k+1) \right) P(k+1|k) \quad (13)$$

where $\hat{\theta}(k+1|k)$ is the state prediction at time $k+1$ given all measurements and estimations up to time k , $\hat{\theta}(k)$ is the optimal state at time k . $P(k+1|k)$ and $P(k+1)$ are a priori and a posteriori covariance matrices associated with predicted and updated state estimates. $z(k+1)$ is the measurement, i.e. calculated angle from frame $k+1$, taken at time $k+1$. Covariance of process noise (C_w) is initialized as 0.01 and covariance of the measurement noise (C_v) is determined experimentally from calculated angles. To initialize the Kalman filter, the optimal state estimate is initialized with $\hat{\theta}(0) = 0$ and a posteriori covariance is initialized as $P(0) = 50$. Results of Kalman filter show that estimations are highly smoothed versions of the calculated angles from images.

B. Scattered Bubble Swarm Analysis

Since acquired shadow images may contain noises and disturbances, simple pre-processing steps are applied to enhance the contrast of image and purify from the noises to distinguish newborn bubbles. Cleaned images are thresholded and labeled via connected component analysis (Fig. 5(b)). Segmented regions are clustered according to area, circumference and centroid properties. The orifice of the probe and main spray flow can be easily distinguishable in these clusters and eliminated. Obtained final image contains only scattered bubble clusters around main flow (Fig. 5(c)).

From 10 to 120 bars inlet pressure level, experiment is repeated and scattered bubbles are extracted. Their distribution

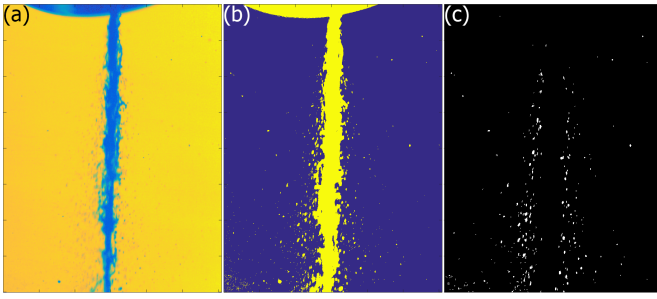


Fig. 5. (a) Exit from the orifice (b) Pre-processed and labelled image (c) Scattered bubbles around main flow

increases close to main flow and forms two peak Gaussian distributions.

To characterize the distributions of these bubbles, modeling the left and right side of bubbles separately as normal distribution and investigation of semi-axis length of ellipse based on covariance matrix is proposed (Fig. 6).

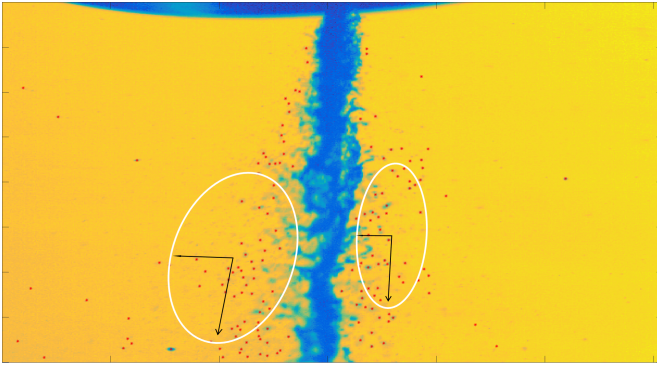


Fig. 6. Scattered bubbles detection and distribution modeling

Axes magnitudes of an ellipse which represents the distribution of bubble centroids, mainly depends on variance of the data. If the axes of this ellipse, parallel to x-y, then equation can be written in terms of standard deviations as:

$$\left(\frac{x}{\sigma_1}\right)^2 + \left(\frac{y}{\sigma_2}\right)^2 = s \quad (14)$$

s is the scale of ellipse, which is related to confidence level according to Chi-Square likelihood [15].

Since bubble distributions can be correlated due to multi-phase flow, the ellipse may not be x-y axis aligned and non-zero covariance may exist. Semi-axis lengths and directions of the ellipse can be determined with eigenvalues and eigenvectors of covariance matrix. Major and minor axis lengths corresponds to square root of largest and smallest eigenvalues ($\lambda_{max}, \lambda_{min}$) of covariance matrix respectively, while their directions are determined by corresponding eigenvectors (v_{max}, v_{min}). Angle between major axes and horizontal axes can be calculated from the largest eigenvector as:

$$\beta = \arctan\left(\frac{v_{max}(y)}{v_{max}(x)}\right) \quad (15)$$

Finally, points on the ellipse can be generated or plotted with the center point (mean of the distributed data) $[X_\mu, Y_\mu]^T$ and $\theta \in [0, 2\pi)$ as:

$$\begin{bmatrix} X_e \\ Y_e \end{bmatrix} = \begin{bmatrix} \cos(\beta) & -\sin(\beta) \\ \sin(\beta) & \cos(\beta) \end{bmatrix} \begin{bmatrix} \sqrt{\lambda_{max}} \cos(\theta) \\ \sqrt{\lambda_{min}} \sin(\theta) \end{bmatrix} + \begin{bmatrix} X_\mu \\ Y_\mu \end{bmatrix} \quad (16)$$

III. EXPERIMENTAL SETUP

Particle Shadow Sizing (PSS) setup (Fig. 7) involves a double shutter high speed CMOS camera (Phantom v310, a trademark of Vision RESEARCH) with 10,000 fps, K2 DistaMax long-distance microscope, Power LED Backlight Illumination Unit, Timing System of PSS to adjust the synchronization of component, LED power and trigger unit and PC.

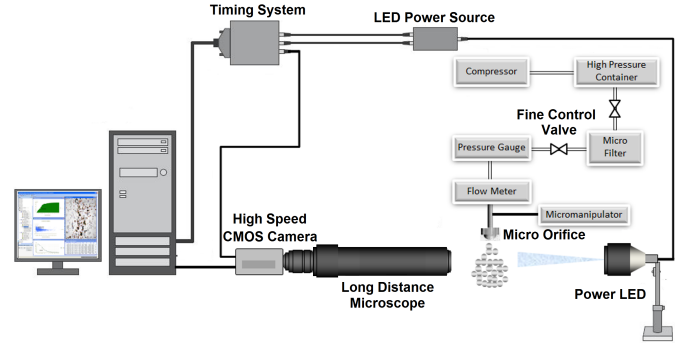


Fig. 7. Experimental setup configuration

Bubbly cavitating flow generator consists of compressor as a pressure source, high pressure container for deionized (DI) water which is also connected to liquid container to keep the input pressure high and guide the fluid through the micro orifice, micro filter for filtering the particles larger than $15 \mu\text{m}$, pressure gauge and flow meter to measure the pressure and finally micro probe which includes 4.5mm short microchannel with $152 \mu\text{m}$ inner diameter.

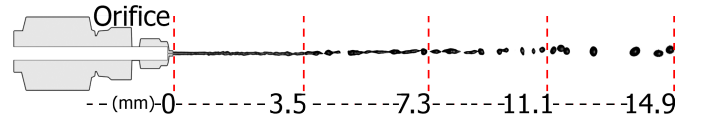


Fig. 8. Flow at different initial pressures was recorded in 4 segments

Experiments are performed with various inlet pressure levels from 10 bars to 120 bar, outlet pressure level is fixed to 1 atm. Since imaging system can monitorize a narrow area such as $4.5\text{mm} \times 6.1 \text{mm}$, flow is recorded in 4 different segments as in Fig. 8.

IV. RESULTS

A. Cone Angle Estimations

For inlet pressure $P_i < 60$ bars, angles are estimated at several cross-sectional area of 3D Gaussian structure. Results in Fig. 9 show that with $P_i = 10$ bars pressure, virtual cone angle can be estimated around 2.1 degrees. Increasing the P_i pressure, leads to increase in cone angle as well. 30 bars inlet

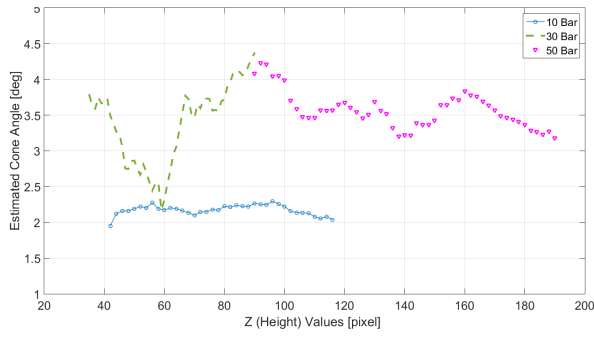


Fig. 9. Estimated cone angles with different inlet pressure (10,30,50 bars)

pressure forms around 3.3 degrees cone angle, whereas the angle is around 3.5 degrees with 50 bars inlet pressure.

With inlet pressure above 60 bars, Kalman filter results show that estimations are highly smoothed versions of the calculated angles from images Fig.10. Average of estimations, exhibit the same behaviour as lower inlet pressures. Increasing pressure above 60 bars to 120 bars, estimated angles reached up to 13 degrees.

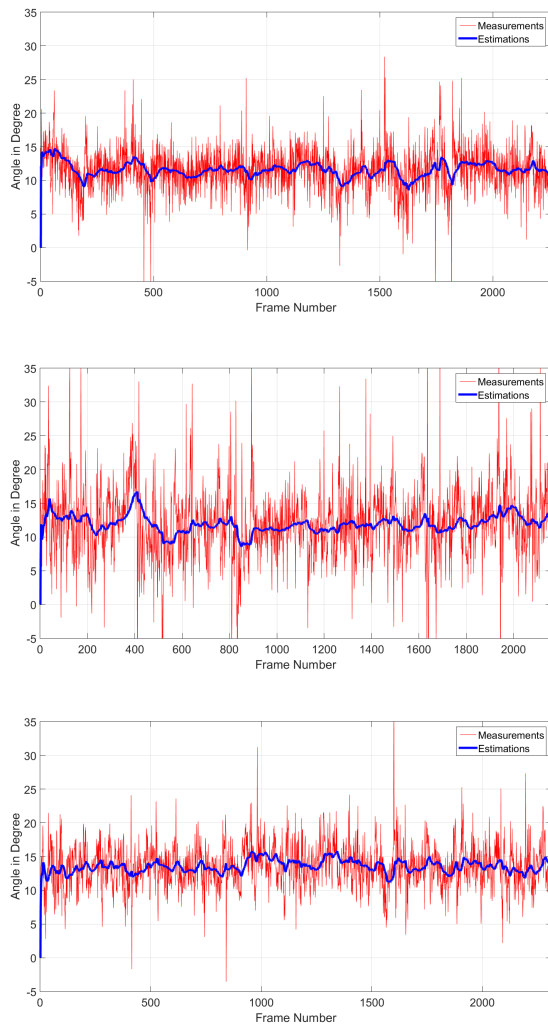


Fig. 10. Estimated cone angle with inlet pressure $P_i=80$, $P_i=100$ and $P_i=120$ bars respectively

Finally, all estimated angles from various inlet pressures from 10 to 120 bars are gathered and showed in Fig.11. Results show that, cone angle of bubbly flow changes with proportional to inlet pressure from 2 to 14 degrees.

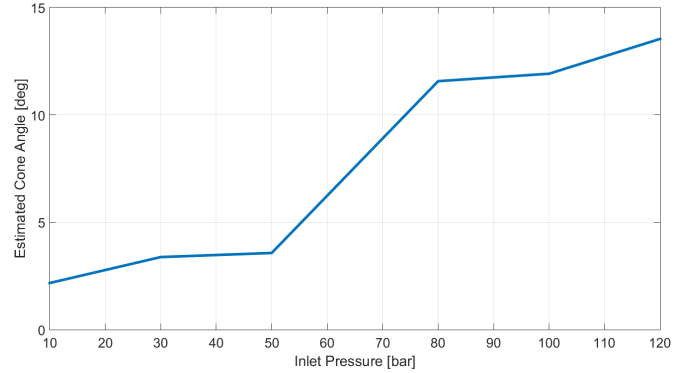


Fig. 11. Estimated angles through 10 to 120 bar inlet pressures

B. Scattered Bubble Distributions

Distribution results of scattered bubbles (Fig 12) show that scattered bubble population is increased with the increasing inlet pressure. These distributions form two-peak Gaussian distributions (Fig. 13). Each peak is investigated separately by covariance matrix of distributed bubble positions. During experiments with inlet pressures between 10 bars to 120 bars, detected bubble areas vary from $30 \mu\text{m}$ to 2 mm.

TABLE I. MAJOR - MINOR AXES PROPERTIES OF BUBBLE DISTRIBUTIONS

Inlet Pressure (bar)	Major Semi-Axes Left (mm)	Major Semi-Axes Right (mm)	Minor Semi-Axes Left (mm)	Minor Semi-Axes Right (mm)
10	1.9430	1.1114	0.3593	0.1858
20	1.6254	1.1174	0.6497	0.4076
30	1.4965	1.1947	0.5549	0.4339
40	1.4188	1.2654	0.4781	0.3747
50	1.3949	1.3383	0.4399	0.3616
60	1.3574	1.3464	0.4031	0.2945
70	1.3545	1.3610	0.4064	0.2909
80	1.3470	1.3600	0.4673	0.3243
90	1.3520	1.3953	0.4385	0.3484
100	1.3784	1.3633	0.4535	0.2575
110	1.3223	1.3969	0.5870	0.3168
120	1.3754	1.3575	0.5558	0.2888

Semi-axes lengths of ellipses obtained from covariance matrices (Table 1) show that major axes lengths are more determinative than minor axes lengths, since they are along the motion of bubbles. When the left major semi-axes lengths increase, corresponding right ones decrease because of the oscillation of bubbly flow generator.

In general, major axes lengths can be considered as decreasing on the average, which shows that more stationary clusters are generated around main flow. Additionally, after a certain pressure level ($P_i > 50$), major and minor axes lengths do not change dramatically. Scattered bubbles are distributed around main flow in the same way but amount of bubbles are increasing (Fig.14).

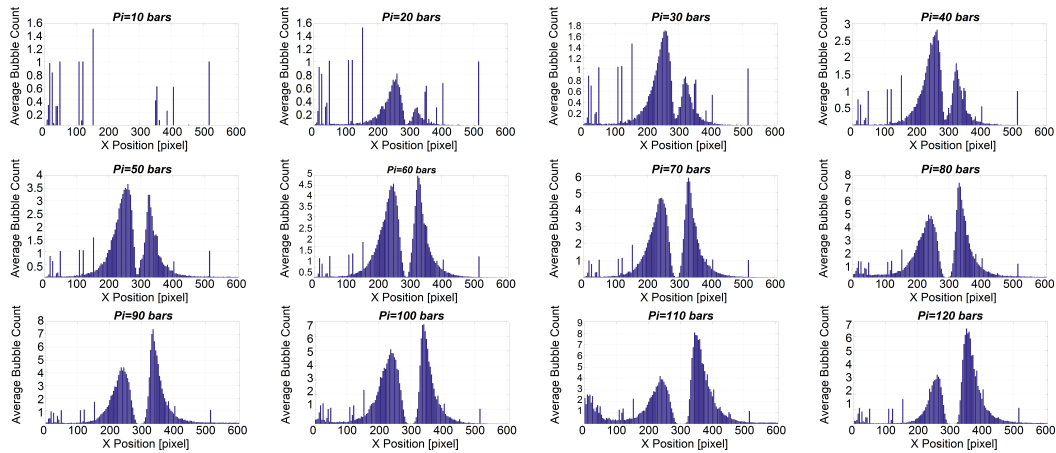


Fig. 12. Scattered bubbles distributions around main flow with different inlet pressure from 10 to 120 bars

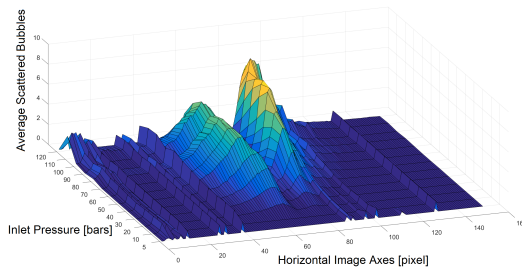


Fig. 13. Obtained two-peak Gaussian distributions

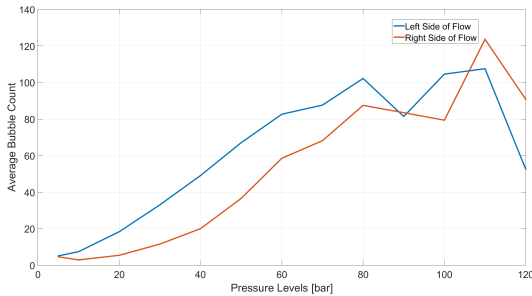


Fig. 14. Scattered bubble counts

V. CONCLUSION

We have now presented two vision based methods to quantify the increasing inlet pressure effect on bubbly cavitating multi-phase flow. First, using a 3D Gaussian model along with recursive filtering, i.e. Kalman filter, angle of the virtually obtained cone is estimated, which is a requisite to position the orifice of bubbly cavitating flow generator during biomedical applications. Second, distributions of scattered bubble swarms around main flow is analyzed with the covariance matrix of bubble positions data. Particle shadow sizing technique is implemented to extract morphological properties of bubbles. Experiments were performed with various inlet pressures from 10 bars to 120 bars and detected bubble diameters varies from 30 μm to 2 mm. Experimental results verify performance of the proposed vision based solutions.

ACKNOWLEDGMENT

This work was supported by TUBITAK (The Scientific and Technological Research Council of Turkey) under Grant No 113S092.

REFERENCES

- [1] Eisenberg, P. Cavitation Damage, Hydraulics. Incorporated Washington, DC, AD No. 602833, 1963.
- [2] Perk, Osman Yavuz, et al. "Kidney stone erosion by micro scale hydrodynamic cavitation and consequent kidney stone treatment." *Annals of biomedical engineering* 40.9 (2012): 1895-1902.
- [3] Itah, Zeynep, et al. "Hydrodynamic cavitation kills prostate cells and ablates benign prostatic hyperplasia tissue." *Experimental Biology and Medicine* (2013): 1535370213503273.
- [4] Bilen, H. and Unel, M. "Micromanipulation using a microassembly workstation with vision and force sensing" (2008) LNCS 5226 1164-1172
- [5] Bilen, H., Hocaoglu, M., Baran, E., Unel, M. and Gozuacik, D. "Novel parameter estimation schemes in microsystems" *IEEE International Conference on Robotics and Automation* (2009) ICRA09 2394-2399
- [6] Bilen, H., Hocaoglu, M., Unel, M. and Sabanovic, A. "Developing robust vision modules for microsystems applications" *Machine Vision and Applications* (20012) 23 25-42
- [7] Adrian, Ronald J., and Jerry Westerweel. *Particle image velocimetry*. Vol. 30. Cambridge University Press, 2011.
- [8] Esteveordal, Jordi, and Larry Goss. "PIV with LED: particle shadow velocimetry (PSV)." 43rd AIAA aerospace sciences meeting and exhibit, meeting papers. 2005.
- [9] Khodaparast, S., N. Borhani, and J. R. Thome. "Application of micro particle shadow velocimetry PSV to two-phase flows in microchannels." *International Journal of Multiphase Flow* 62 (2014): 123-133.
- [10] Bian, Yuchen, et al. "3D reconstruction of single rising bubble in water using digital image processing and characteristic matrix." *Particuology* 11.2 (2013): 170-183.
- [11] Zhang, Wen-Hui, Xiaoya Jiang, and Yin-Mingzi Liu. "A method for recognizing overlapping elliptical bubbles in bubble image." *Pattern Recognition Letters* 33.12 (2012): 1543-1548.
- [12] Bailey, M., C. O. Gomez, and J. A. Finch. "Development and application of an image analysis method for wide bubble size distributions." *Minerals engineering* 18.12 (2005): 1214-1221.
- [13] Otsu, Nobuyuki. "A threshold selection method from gray-level histograms." *Automatica* 11.285-296 (1975): 23-27.
- [14] Maybeck, P.S. "Stochastic models, estimation and control", Volume I, Academic Press, Inc., 1979.
- [15] H.O. Lancaster, "The chi-squared distribution", Wiley (1969)